

## Load monitoring of a cantilever plate by a novel multimodal fibre optic sensing configuration

Nazeer, N.; Groves, R. M.

**DOI**

[10.1007/s42452-021-04663-9](https://doi.org/10.1007/s42452-021-04663-9)

**Publication date**

2021

**Document Version**

Final published version

**Published in**

SN Applied Sciences

**Citation (APA)**

Nazeer, N., & Groves, R. M. (2021). Load monitoring of a cantilever plate by a novel multimodal fibre optic sensing configuration. *SN Applied Sciences*, 3(6), Article 667. <https://doi.org/10.1007/s42452-021-04663-9>

**Important note**

To cite this publication, please use the final published version (if applicable).  
Please check the document version above.

**Copyright**

Other than for strictly personal use, it is not permitted to download, forward or distribute the text or part of it, without the consent of the author(s) and/or copyright holder(s), unless the work is under an open content license such as Creative Commons.

**Takedown policy**

Please contact us and provide details if you believe this document breaches copyrights.  
We will remove access to the work immediately and investigate your claim.



# Load monitoring of a cantilever plate by a novel multimodal fibre optic sensing configuration

N. Nazeer<sup>1</sup> · R. M. Groves<sup>1</sup>

Received: 3 November 2020 / Accepted: 13 May 2021

Published online: 27 May 2021

© The Author(s) 2021 [OPEN](#)

## Abstract

Optical fibre sensors and in particular fibre Bragg gratings (FBG) have received a lot of interest for Structural Health Monitoring in different application fields, such as aerospace, pipeline and civil engineering. FBGs are conventionally used to monitor strain and sometimes temperature. In this paper, we propose a new method for load monitoring of a cantilever plate subjected to point loading. The bending of plate is complex due to the interaction between the axial and transverse bending stiffnesses of the material. We use a novel algorithm for interrogating fibre Bragg grating sensors based on both hybrid interferometry and FBG spectral sensing. The method is demonstrated in this paper using a single-mode optical fibre containing four FBG sensors to estimate both the point loading position and the loading magnitude at an arbitrary location on a 1 m<sup>2</sup> cantilever plate. The algorithm first utilizes point strain information through spectral sensing as well as strain from interferometric sensing over a long path. The gratings are interrogated using Wavelength Division Multiplexing (WDM). We calibrated the system using an experimental model. This model was then verified by using single point static loading tests and comparing the calculated sensing position with the actual position. The method achieved a good estimation of loading position achieving a measurement error of about 9% in a 2D plane. The analysis discusses the possible sources of inaccuracies. This study forms the basis of our future work involving morphing smart-wing sections for the purpose of load monitoring.

## Article highlights

- A new optical sensing configuration is demonstrated for load and structural health monitoring of cantilever structures.
- The algorithm successfully estimates the position of an arbitrary load on a cantilever plate, with an error of 9%.
- This methodology will be extended to monitor more complex structures, including morphing aircraft wing sections.

**Keywords** Structural health monitoring · Optical fibre sensing · Multimodal sensing · Cantilever plate · Shape sensing

## 1 Introduction

Structural Health Monitoring (SHM) has been extensively used to keep track of the structural integrity of engineering structures including those in aerospace [1, 2], wind

turbine blades [3], pipelines [4] and in civil engineering [5–7]. Apart from increasing safety, SHM also plays a role in substantially reducing the cost of inspection and maintenance whilst improving operational reliability and reducing downtime. This helps in making sure the

✉ N. Nazeer, N.Nazeer@tudelft.nl; R. M. Groves, R.M.Groves@tudelft.nl | <sup>1</sup>Aerospace NDT Laboratory, Faculty of Aerospace Engineering, Delft University of Technology, Kluyverweg 1, 2629 HS Delft, The Netherlands.



structure is working within its intended structural limits throughout its working life [8].

Aircraft wings are constantly subjected to bending and torsional deformations due to aerodynamic loading and these loads must be kept within the design limit of the structure [9]. Monitoring these loads is the first level of SHM [10].

In addition to the structural integrity aspect, changes in shape also change the aerodynamic performance of the wing, which in turn leads to a further change in aerodynamic loads on the structure. In a passive system, knowledge of the relationship between aerodynamic loading and wing deformation can lead to improvements in structural design that can potentially improve fuel economy and structural safety.

The most widely used example for a wing failure due to lack of load monitoring is NASA's flight test of helios in 2003 [11]. A failure to monitor the structural loads acting on the wings and the related shape deformation resulted in the wings to fail and collapse. Following this, efforts have been put in to come up with different wing deformation monitoring solutions [12, 13].

Considering the size, sensitivity and immunity to electrical noise in the environment, optical fibres are the preferred technology for smart sensing applications [14]. Moreover, due to their unobtrusive nature they can also be either bonded on to structures or even embedded in composites without affecting their structural integrity. Over the years, different optical fibre-based curvature sensors and sensing methods have been investigated but their applications remain mostly limited and within the laboratory environment.

Shape sensing is predominant in the medical field with the help of arrays of FGB sensors [15] as well as with distributed fibre optic sensing [16]. Recently, a multi-fibre approach was also demonstrated for beam bend sensing for medical applications. [17]. Deformation measurements on larger structures including full scale wings have been reported using an array of fibres with densely populated FBGs [12, 18]. The Inverse Finite Element (IFEM) method [19] has also interested researchers for shape sensing and a comparative study [20] has also been carried out showcasing its benefits over other methods. Overall, the primary aims of these methods are curvature or bend sensing whilst none give information on the location of the load being applied [21–23].

This work is part of the morphing wing technology project SmartX. The SmartX wing contains independent morphing flaps/sections. Load monitoring of these sections is crucial during its flight regime. The objective of this work in the wider project is to determine the location of an arbitrary load, the magnitude of the load and to translate this information to obtain the deformed shape.

Considering the first step in the process, our aim was to develop a simple sensing method that does not require complex and intricate manufacturing procedures [24–26] or involve a large array of sensors [13, 27].

Although this method could be applied on any plate-like structure that undergoes bending and torsion, the focus of this paper is steered towards aircraft wings and wing subsections. Additionally, we first investigate only concentrated point loads. A preliminary study of the potential of this approach was reported earlier by us for a one-dimensional case [28] and the results presented here are an extension of this study.

The structure of the paper is as follows. Section 2 presents the theory of the proposed method. Section 3 introduces the principle of the approach and describes the experimental setup including the geometry and sensor design. Section 4 introduces the calibration steps, measurements and the algorithm. This is then followed by the results in Sect. 5. Section 6 discusses the findings and finally, Sect. 7 concludes the paper.

## 2 Theory

This work makes use of the principles of both spectral and interferometric sensing for fibre Bragg gratings (FBGs).

### 2.1 FBG spectral sensing principle

Grating-based optical fibre sensors function on the principle of Bragg reflection [9]. The Bragg grating, (of length  $L_{FBG}$  as shown in Fig. 1), forms the sensing region which acts as a bandpass filter in reflection and a bandstop filter in transmission at the Bragg wavelength.

Gratings are inscribed in the fibre with a laser by using a phase mask to form a specific spatial pattern. Photosensitive fibres are typically used so that the refractive index (RI) of the core could be modified easily by laser light [29]. These gratings usually have a length of 1 mm to 20 mm with a submicron period ( $\Lambda$ ) and selectively

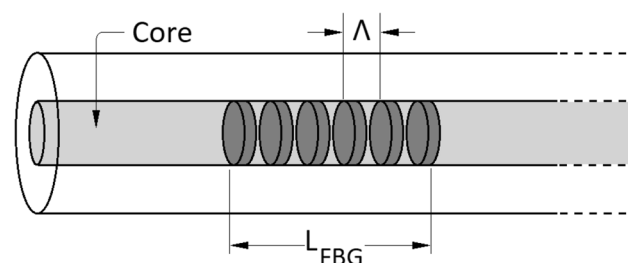


**Fig. 1** Structure of a fibre Bragg grating (FBG) sensor.  $L_{FBG}$  is the sensor length and  $\Lambda$  is the grating period

couple a narrow spectral band of light from the forward-propagating mode to the counter propagating mode [30].

The Bragg wavelength [31] is given by:

$$\lambda_B = 2n_{eff} \Lambda \quad (1)$$

where  $n_{eff}$  is the refractive index of the core and  $\Lambda$  is the periodic spacing of the grating. As  $\lambda_B$  is a function of the RI and grating period, the Bragg wavelength shifts when the gratings are subjected to external mechanical and thermal changes. The wavelength shift caused by a change in strain and temperature is denoted by  $\Delta\lambda_B$  and the strain can be expressed as a shift in the Bragg wavelength as [32]:

$$\Delta\epsilon = \frac{\Delta\lambda_B}{\lambda_B(1 - \rho_a)} - \Delta T(\alpha_n + \frac{\xi}{(1 - \rho_a)}) \quad (2)$$

where  $\Delta\epsilon$  is the calculated strain,  $\rho_a$  is the photoelastic coefficient,  $\alpha$  is the thermal expansion coefficient,  $\xi$  is the thermo-optic coefficient and  $\Delta T$  the change in ambient temperature.

FBG interrogators contain photodetectors that compare the light reflected from the gratings with a wavelength reference in order to determine the position of the centre wavelength. This information is converted from magnitude of wavelength shift to a value in terms of strain (typically  $\mu\epsilon$ ).

Figure 2 shows the spectra obtained through FBG spectral sensing during a static bend test on the plate. Four peaks are achieved corresponding to four FBGs in the fibre. Shift in the Bragg wavelengths are observed for the first ( $\Delta\lambda_{B1}$ ) and fourth ( $\Delta\lambda_{B4}$ ) peaks as they undergo tension unlike the second and third peaks. Using equation 2, the strain at the FBG location is calculated.

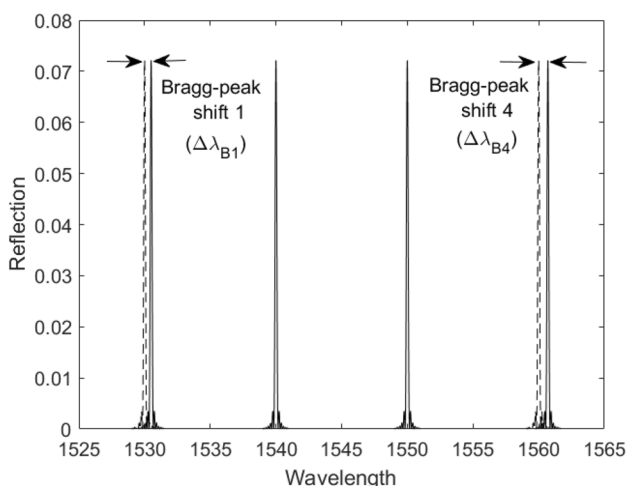


**Fig. 2** Bragg shifts  $\Delta\lambda_{B1}$  and  $\Delta\lambda_{B4}$  of the first and fourth peaks due to the plate undergoing static bending

## 2.2 FBG-Pair interferometric sensing principle

The FBG-Pair sensing used is based on the principle of measuring phase differences caused by interference patterns in a measurement zone [33]. A zone is defined as a region in the optical fibre between two partially reflecting mirrors. In this case, the gratings themselves act as reflectors.

The two FBGs (for example,  $FBG_1$  and  $FBG_2$ ) that form a zone in the sensing fibre reflect light at the Bragg wavelengths of these two FBGs. In parallel, light from a reference optical fibre is reflected by a reference element (mirror). The reflected portion of light from the sensing fibre and the reference fibre are combined to produce interference patterns that are resolved into phase information.

The phase signal represents the optical path length of the zone and is sensitive to changes in strain and/or temperature between the gratings. The length of the zone changes in the presence of any external perturbation, and this change in zone length ( $\Delta l$ ) is given by:

$$\Delta l = L_{sensor}\epsilon + L_t\Delta T \quad (3)$$

where  $L_{sensor}$  is the length between the gratings that forms the effective sensing zone,  $\epsilon$  the calculated strain,  $\Delta T$  the change in ambient temperature and  $L_t$  the change zone length due to temperature. The strain from the zone henceforth will be calculated as:

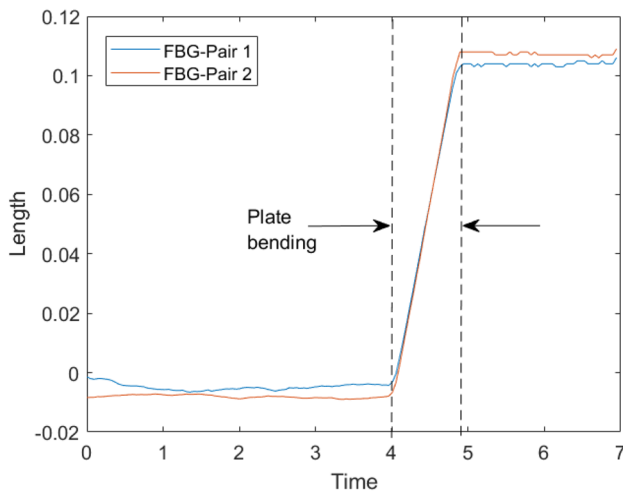
$$\epsilon = \frac{\Delta l - L_t\Delta T}{L_{sensor}} \quad (4)$$

Figure 3 shows the spectra obtained through FBG-Pair interferometric sensing during a static bend test on the plate. Each spectrum corresponds to an FBG Pair. The spectra are identical to each other as the plate undergoes bending. Using Equation 4, the change in zone length ( $\Delta l$ ) is calculated.

## 2.3 Multimodal sensing principle

The principle of this sensing method is based on the combination of FBG spectral sensing (Sect. 2.1) and FBG-Pair interferometry (Sect. 2.2). This follows a two-step measurement procedure.

For the first step, the spectral shift of each grating is measured and translated to strain which can be acquired through equation 2. As for the second step, the optical distance between two given gratings is measured and the strain is acquired using equation 4. For the second step, for a one-dimensional case, the requirement of the number of grating sensors is 2 [28]. The number of gratings required is always an even number as the interferometric sensing is



**Fig. 3** Change in zone length  $L_{sensor}$  between two FBGs due to the plate undergoing static bending

always between grating pairs. Each of the gratings have a distinct centre wavelengths interrogated through the Wavelength Division Multiplexing (WDM) approach. The reflector gratings are as shown in the zoomed-in segment in Fig. 5, Sect. 3.1. The reflected light (from two gratings) from the sensing fibre and the reference fibre is combined to produce two spectrally distinctive interference patterns; the first pattern is based on light components of the first grating’s wavelength and a second based on the second wavelength. This interference pattern is resolved into the phase difference information. This phase difference varies with the length ( $L$ ) and the acquired information indicates the displacement between the two gratings. The resultant displacement ( $\Delta L$ ) between the gratings due to this phase difference is hence given by:

$$\Delta L = \frac{1}{n} \left[ \left( \frac{\Delta \Phi \lambda}{2\pi} \right) - L \Delta n \right] \tag{5}$$

where  $n$  is the refractive index,  $\Phi$  is the phase difference and  $\lambda$  is the wavelength at which the grating reflects light. This is used to acquire the strain between the selected grating pairs using equation 4.

Finally, the analysis of the measurements is done with the strain information from each grating combined with the displacement information between each grating pair. The step-by-step implementation of these two measurements to predict the location and magnitude is further explained with the algorithm (Sect. 4.3).

### 3 Experimental setup

#### 3.1 Geometry

A schematic of the test specimen is shown in Fig. 4, and this figure also defines the coordinate system and nomenclature used. The plate’s length is along the x-axis and the breadth (clamped side) along the y-axis. The test specimen was an aluminium plate of length  $l = 1000$  mm, breadth  $b = 1000$  mm and thickness  $t = 2$  mm, bolted on one side to an aluminium beam (Boikon) ( $l = 1100$  mm,  $b = 40$  mm, and  $t = 40$  mm), which is in turn bolted to the optical table. These dimensions were chosen to be able to have a better understanding of realistic sized measurements as these findings would be translated to a similar sized morphing wing section for our future work. For practical reasons, the plate was clamped vertically unlike a typical cantilever setup as we sought to minimize gravitational loads in the x-y plane. The plate in an unloaded state manifested uneven curves as the cutting and clamping process introduced residual stresses and curvature. The clamped and the free ends will further be referred to as the root and the tip, respectively. The force ( $F$ ) deflection applied is in the (thickness direction) negative z-axis. A linear actuator (Zaber, NA23C60-T4) and controller stage allowing a deflection range of 0 to 60 mm were affixed onto a base plate mounted on a horizontal and vertical slider. The actuator deflects the plate at different points on the plate. The slider mechanism provides ease in sliding the actuator to the desired test point.

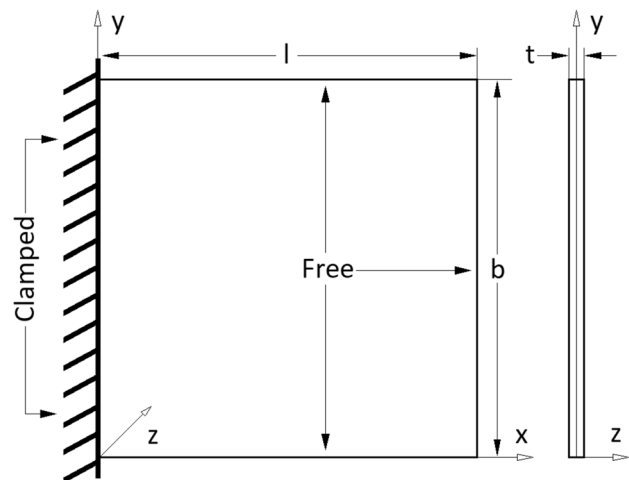
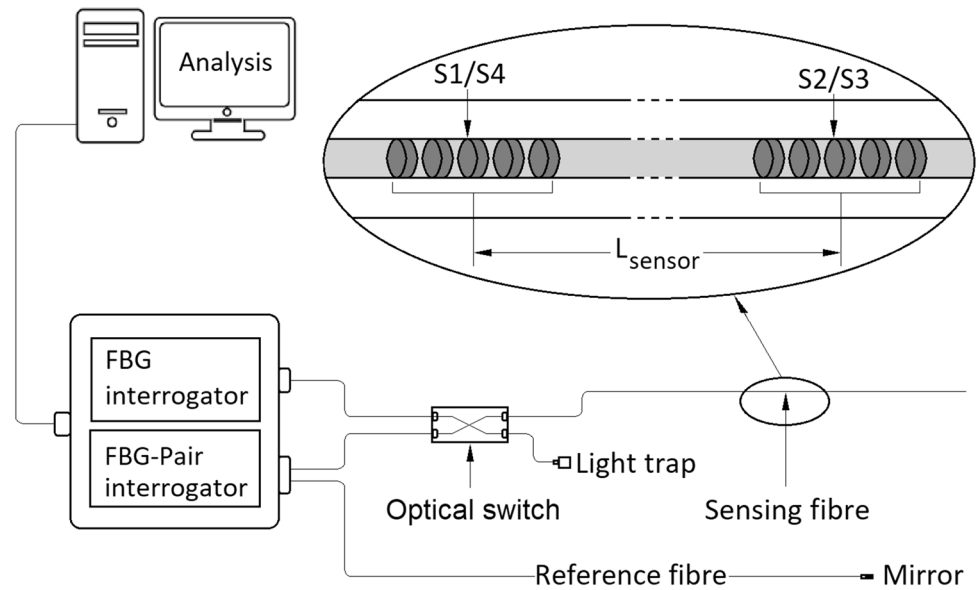


**Fig. 4** Diagram and definition of the coordinate system of the setup including the boundary conditions. The plate has length  $l$ , breadth  $b$ , and thickness  $t$ . One side is clamped and the others are left free. The plate is free to move in the  $\pm z$ -axis, away from the clamped side

**Fig. 5** Schematic of the experiment including the two interrogators, the sensing fibre and the reference fibre. Zoomed in: Structure of the sensing fibre containing gratings S1 or S4 and S2 or S3 as reflectors. The distance between the grating pairs is marked as  $L_{\text{sensor}}$



### 3.2 Setup

Figure 5 shows the schematic of the experiment used to carry out this study. An optical sensor FBG-Pair interrogator (Optics11, ZonaSens) measured the displacement between S1-S2 and S3-S4 grating pairs for each test case. A second measurement system, a spectral FBG interrogator (National Instruments, PXIe-4844), measured the local strain at each of the FBGs. Both the interrogators have a tunable wavelength-swept laser and a class 1M laser. As both the interrogators have their own light sources,

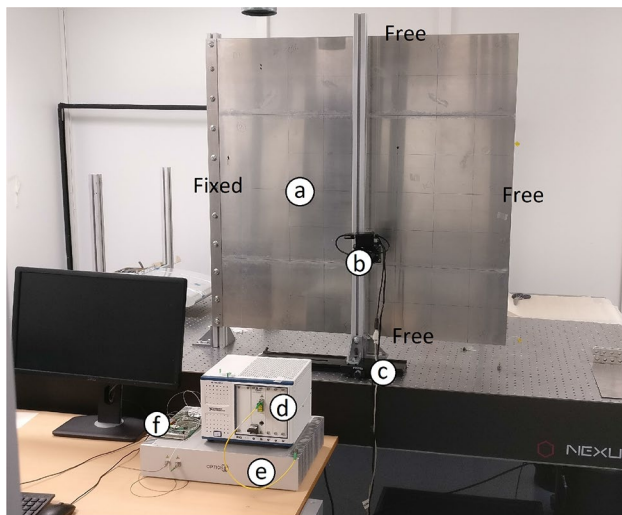


**Fig. 6** Laboratory setup of the experimental study containing the **a** cantilever plate, **b** linear displacement stage actuator, **c** slider setup for the linear actuator, **d** National Instruments interrogator, **e** optics11 interrogator and the **f** Thorlabs optical switch is displayed

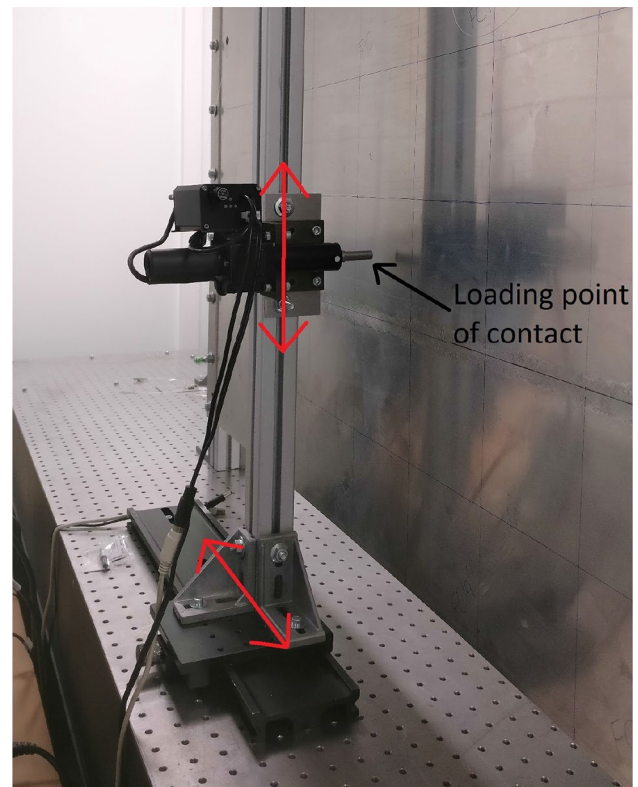


**Fig. 7** Loading setup showing the vertical and horizontal slider mechanism for the linear actuator

interrogating the same fibre simultaneously caused erroneous measurements. To overcome this, an optical switch (Thorlabs, OSW22-1310E) was used to select the interrogator system in use. A switching-technique was incorporated

to measure simultaneously with both the interrogators. The wavelength resolution of the FBG interrogator is 4 pm and of the FBG-Pair interrogator is 1 pm. The sensing fibre is bonded on the plate under test.

Figure 6 shows the experimental setup including the plate. The plate stands similar to a flag, bolted on one side and left free at the others.

The loading procedure was carried out with the linear actuator connected to a vertical support as shown in Fig. 7. The bottom slider fixed to the optical table helped in moving the actuator from  $x = 500$  to  $1000$  mm. The vertical slider was used to cover distances from  $y = 0$  mm to  $1000$  mm.

### 3.3 Sensor design

Determination of the optimal location of the sensors is beyond the ambit of this work. The chosen location was partly derived from the location optimization performed by Jones et al. [23] and Ko et al. [12] on a similar cantilever bending case. The fibre was laid out along the length of the plate in a U-shape pattern in such a way that (the FBG sensors) S1 and S4 were positioned near the root and S2 and S3 near the tip. The fibre containing the FBGs was bonded to the surface of the plate using cyanoacrylate adhesive (3M Scotch-Weld) except the length between S2 and S3. This length had no consequence on the measurements and was simply taped to the plate. The sensors were oriented perpendicular to the y-axis so that the gratings

were perpendicular to the axis of bending. S1 and S4 on the cantilever plate are at approximately  $x = 50$  mm from the root and S2 and S3 at  $x = 950$  mm from the root and measure the normal strains acting in the clamped-free direction. The length between the two grating pairs,  $L_{sensor}$  formed the effective sensing zone as shown in Fig. 5. The interrogation system allows  $L_{sensor}$  to be up to several metres. In this case  $L_{sensor}$  was  $0.9$  m. The location of the sensors on the plate is as shown in Fig. 8. Measurement of change in length between grating sensors S1 and S2 is given by  $\Delta L_{1-2}$  and between gratings S3 and S4 by  $\Delta L_{3-4}$ . Local strain measurements are given as corresponding to their sensor numbers (ref. Fig. 8), as  $\epsilon_1, \epsilon_2, \epsilon_3$  and  $\epsilon_4$  from sensors S1, S2, S3 and S4, respectively. As the plate had a negligible thickness compared to its length the shear strains are not considered here. Furthermore, sensors S2 and S3 are near the free end of the cantilever. This would make  $\epsilon_2$  and  $\epsilon_3$  very small in magnitude compared to  $\epsilon_1$  and  $\epsilon_4$ . Additionally, these measurements would show no reading for low deflection cases and are hence not taken into account in the final estimation.

The gratings were inscribed in a standard single mode SMF-28e (Corning)-type fibre. Their properties are listed in Table 1 as specified by the manufacturer (DK Photonics). The wavelengths were selectively chosen as the two interrogators work within the C-band range. The gratings were 3 mm long each with bandwidth and reflectivity levels above 0.75 nm and 97%, respectively, and temperature sensitivity of  $10$  pm/°C.

## 4 Measurements

### 4.1 Calibration

This measurement technique requires initial calibration of the test specimen and the development of an experimental based model.

To have a realistic yet simple set of measurements, the plate was initially divided into a 9x9 grid making every single grid square 125 x 125 mm. The deflections were recorded only on the tip-end half of the plate within a 5x9 grid (45 points), see Fig. 9. These 45 points were taken as

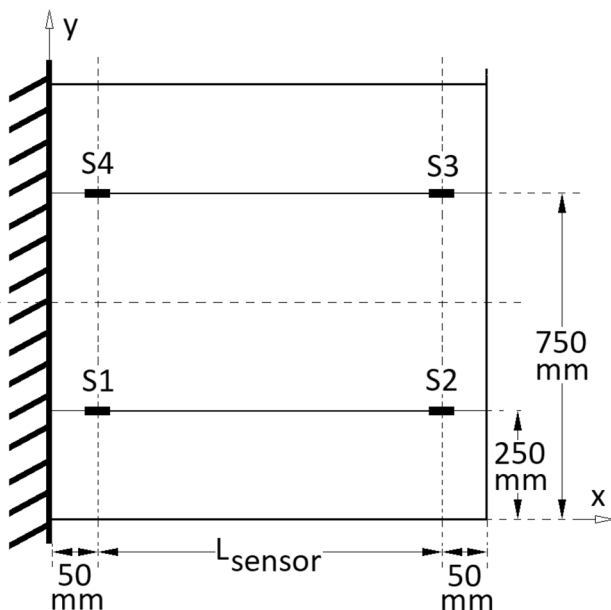
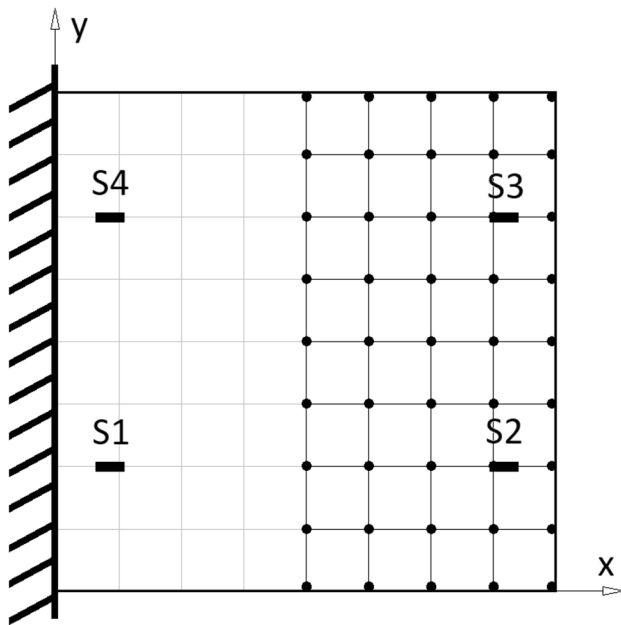


Fig. 8 Location of the sensors on the plate. S1-S2 and S3-S4 run in the clamped-free direction and are parallel to the central axis. The sensor pairs are 250 mm and 750 mm from the origin, respectively

Table 1 Properties of the grating sensors S1, S2, S3 and S4 (DK Photonics)

Property	S1	S2	S3	S4
Wavelength	1530.182 nm	1539.903 nm	1549.955 nm	1560.118 nm
Bandwidth	0.785 nm	0.762 nm	0.785 nm	0.782 nm
Reflectivity	98.27%	98.12%	98.32	97.42%



**Fig. 9** Chosen grid highlighted on one section of the plate where all measurements are carried out. Each point on the grid corresponds to a calibration point. The four grating sensor positions also marked

calibration points for future measurements. To account for larger deflections, measurements  $\Delta L_{1-2}$ ,  $\Delta L_{3-4}$ ,  $\epsilon_1$  and  $\epsilon_4$  for up to 25 mm deflection were recorded. The results discussed are for steps of 5 mm (0, 5, 10, 15, and 25 mm) up to 25 mm as this was the estimated deflection range of the wing segment for our follow-up work involving multiple morphing wing sections.

Points closer to the root are not considered because a) The 45 points within  $x = 500$  mm to 1000 mm amount to the total points in the free half of the plate grid that fall in the loading area of interest in this study, and b) larger deflections within  $x = 0$  mm to 500 mm cause the plate to undergo complex bending (Refer to Sect. 3) that is out of the focus of this study.

Additionally, to understand the dependence of calibration-point number, location and grid density a second set of measurements were carried out on a coarser 3x3 reference-grid pattern (see Sect. 5.2) for the same specimen. This was just to show the difference when a coarser grid was used. Investigation on the ideal grid spacing would require a further grid size convergence study and is not looked into in this paper.

## 4.2 Deflection at arbitrary locations

To have a deeper understanding of plate deflections due to loads at unknown positions, arbitrary locations with respect to the grid were measured.

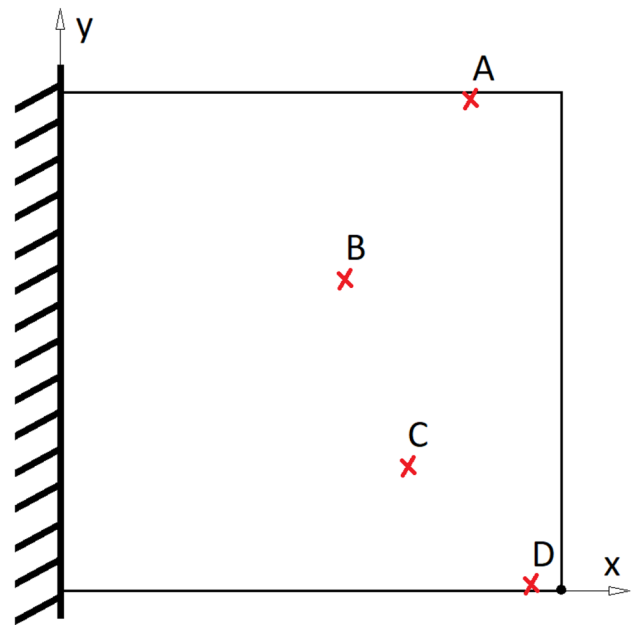


**Fig. 10** Location of arbitrary test points A to D measured at (812,995), (562,620), (687,255) and (937,5)  $\pm 2$  mm, respectively

The fibres are 250 mm away on either side of the plate's axis of symmetry. To a first approximation, the bending component should follow the beam model [28]. There should be no torsion when the load is applied on the centreline of symmetry, and as a result  $\Delta L_{1-2}$  and  $\epsilon_1$  should be the same as  $\Delta L_{3-4}$  and  $\epsilon_4$ , respectively.

### 4.2.1 Test 1—Finer grid

Deflections of 0 to 25 mm in steps of 5 mm were applied with the linear actuator at 4 arbitrary locations. These arbitrary locations are marked as A, B, C and D on the plate and are at the (x,y) locations (812,995), (562,620), (687,255) and (937,5) mm, respectively, as shown in Fig. 10. To record the repeatability, six trials were taken for each deflection step. This means that for a single and each deflection step the plate was loaded/unloaded six times. The loading location accuracy is estimated as  $\pm 2$  mm. The loading point was a flat circular surface of radius 5 mm, marked as 'loading point of contact' in Fig. 7. The strain along the length  $\Delta L_{1-2}$  and  $\Delta L_{3-4}$  and the point strain measurements  $\epsilon_1$  and  $\epsilon_4$  are recorded.

### 4.2.2 Test 2—Coarser grid

The calibration and recording of reference points was followed by the same setup and procedure as the previous experiment except that a coarser grid was used as shown in Fig. 11. The location accuracy again is estimated as  $\pm 2$  mm.



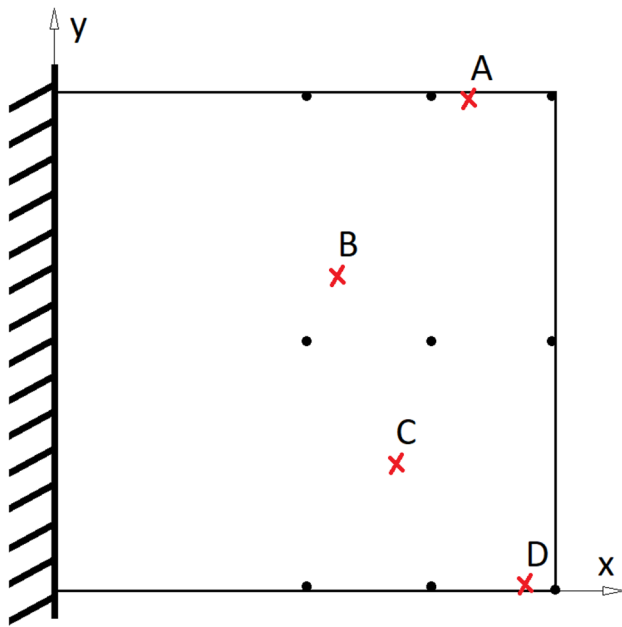


Fig. 11 Location of arbitrary test points A to D on a coarser calibration grid

### 4.3 Algorithm

The algorithm used basically relies on linear interpolation between predetermined fixed reference points, referred here as calibration points (CP). For each reference point, sum of the strains is calculated for each sensor. The algorithm used deals with predicting the location of load applied on a surface from a sparse set of sensors. A simple data-driven algorithm is presented to tackle this challenge.

Each grating sensor in the experiment provides a measurement reading ( $\epsilon_1, \epsilon_4$ ). On the other hand, each grating sensor pair provides an additional set of readings ( $\Delta L_{1-2}, \Delta L_{3-4}$ ). The combined value of all the sensors is mapped to a particular location on the surface which is what estimates the loading location.

Step 1: Calibration data are recorded for the 45 grid points as shown in Fig. 9. These data points would serve as baseline measurements. Calibration Points (CP) are calculated by applying a load at a known location and recording all sensor measurements. Step 2: Deflection on an unknown location (as shown in Fig. 10) called arbitrary Test Point (TP) is applied, and the resulting measurement data for all the sensors are recorded.

From step 1, CP measurement values  $\Delta L_{1-2}, \Delta L_{3-4}, \epsilon_1$  and  $\epsilon_4$  are recorded for each corresponding variable and each corresponding CP. That is, CP measurements each of  $\Delta L_{1-2}, \Delta L_{3-4}, \epsilon_1$  and  $\epsilon_4$  for points 1 to  $n$ .  $n$  here represents the reference CP number (45 CP points, refer Sect. 4.1 and Fig. 9). These are the reference point data.

**Table 2** Measurements  $\Delta L_{1-2}, \Delta L_{3-4}, \epsilon_1$  and  $\epsilon_4$  with six repeats for a 20 mm displacement at the centre of the plate ( $x = 500$  mm,  $y = 500$  mm) are shown.  $\Delta L$  values are in microns and  $\epsilon$  values are in microstrain

$\Delta L_{1-2}$	$\Delta L_{3-4}$	$\epsilon_1$	$\epsilon_4$
68.79	55.28	110.58	129.02
68.82	55.25	110.57	128.99
68.74	55.32	110.59	128.99
68.74	55.22	110.58	129.01
68.83	55.28	110.59	129.02
68.80	55.24	110.61	129.02

Next, from step 2,  $\Delta L_{1-2}, \Delta L_{3-4}, \epsilon_1$  and  $\epsilon_4$  from load at an arbitrary TP are recorded.

Step 3: Each of the CP data from step 1 is divided by the TP data from step 2; (CP  $\Delta L_{1-2}$  for point 1 / TP  $\Delta L_{1-2}$ ) ... (CP  $\Delta L_{1-2}$  for point 45 / TP  $\Delta L_{1-2}$ ). The percentages of these ratios are denoted as  $k1_n$  for all  $\Delta L_{1-2}, k2_n$  for all  $\Delta L_{3-4}, k3_n$  for all  $\epsilon_1$ , and  $k4_n$  for all  $\epsilon_4$ .

Step 4: Sum of  $k1_n, k2_n, k3_n$ , and  $k4_n$  for points 1 to  $n$ . This is denoted by capital  $K_n$ . This would result in 45  $K_n$  values.

i.e.  $K_n$  is calculated for every variable for  $1 \leq n \leq 45$  as:

$$K_n = (\sum k1_n + k2_n + k3_n + k4_n)/4 \tag{6}$$

When the TP coincides with the CP,  $k1_n, k2_n, k3_n$ , and  $k4_n$  would be 1 and the percentages of these values would be equal to 100. Following equation 6, capital  $K_n$  would hence be 400/4. This means that in an ideal case  $K_n$  is equal to 100, indicating that the loading point is exactly at the reference point 'n'.

In the case when the TP does not coincide with the CP, the value of  $K_n$  is either greater or lower than 100. Due to the calibration grid shape (refer Fig. 9), the TP always falls inside any one of the calibration grid-boxes. This means that there are four closest CP's surrounding the TP. Our aim is hence to locate the point within the grid-box that coincides with  $K_n = 100 (\pm 1.5, \text{for increased tolerance and resolution})$ . For this an interpolation is done between all the adjacent points and the TP. This reveals a closed region marked in black that is the estimate of the probable location of the applied load.

The location of this TP is now a new CP for the learning algorithm and is now considered as an additional point in the calibration grid. In other words, the original grid number of  $n = 45$  increases by 1 and the new range is  $1 \leq n \leq 46$ . The value of 'n' keeps increasing after every new TP is measured hence increasing the CP data library of the algorithm.

The converse of the above approach can be used to estimate the deflection magnitude keeping it as an unknown variable. The values of  $\Delta L_{1-2}, \Delta L_{3-4}, \epsilon_1$  and  $\epsilon_4$  measured at each step of the tests are stored as calibration data. These

steps create a database that would be used to back-calculate the deflection magnitude.

## 5 Results

As an example, the typical magnitude of acquired strains is shown in Table 2 for displacement applied at the centre of the plate ( $x = 500$  mm,  $y = 500$  mm). For each loading case, six trials were recorded. The measurements carried out for  $\Delta L$  and  $\varepsilon$  were within the 0 to 85 and 0 to 160 microns region, respectively.

It is to be noted that measurements  $\varepsilon_2$  and  $\varepsilon_3$  from sensors S2 and S3, respectively, were not taken into account in the algorithm. For low deflections, the magnitudes of  $\varepsilon_2$  and  $\varepsilon_3$  were less than 5% and for higher deflections (up to 30 mm) up to a maximum of 16% relative to  $\varepsilon_1$  and  $\varepsilon_4$ .

The measured standard deviation for measurements is 0.035, 0.038, 0.012 and 0.013, respectively. This measurement accuracy has an effect of  $\pm 1.5$  on the output quantity  $K_n$  (equation 6) which is already considered in the algorithm step (Sect. 4.3) while estimating the region of loading.

### 5.1 Finer grid

The acquired plate surface position estimations for test points A to D are displayed as follows. For each test point, the plate map for all the deflection cases is shown individually. There are five deflection cases (5 mm to 25 mm in steps of 5) for each test point. Figures 12, 13, 14 and 15 show the deflections for test points A, B, C and D, respectively. These cases are shown for the finer (5x9) grid case, refer to Sect. 4.2.1.

The region between 100 to 120 on the colour bar is represented by shades of green on the plate's surface. The algorithm identifies and shades the area closest to the 100 mark in black with a tolerance limit of up to 1.5. This chosen tolerance limit makes the area larger but helps in providing a better resolution for marking the region. The shaded portion typically forms a closed form region denoting the point of interest to be anywhere within it.

For test point A (Fig. 12), the estimated region goes beyond the plate in the positive y direction. As there are no further reference points past the boundary, the region has an open pattern with straight line edges. The plate at this point is bent in a state of torsion with the plate deflected at the marked region. For lower deflections, the estimated region remains the same but starts to become bigger (indicating increase in estimated-region prediction error) for deflections above 20 mm. With the increase in deflection magnitude, we also notice the colour map

across the plate shifting more towards shades of orange, yellow (and green).

Test points B (Fig. 13) and C (Fig. 14), on the other hand, are in the mid-region of the plate and consequently have a closed form pattern as there are reference points in all directions. In these two cases, the increase in the error across the plate is more prominent going from lower to higher deflections. This is indicative by the colour shifting rapidly towards yellow in the colour bar for regions away from the loading point. The estimated region also gets bigger for deflections greater than 15 mm.

For the same reason as for point A, the open pattern is also seen in test point D (Fig. 15) which is again a corner point. The plate in this case predominantly also undergoes torsion with the highest deflection near the marked region.

The measured load points are within the estimated region for the arbitrary locations A and D. The sizes of these estimated regions are within a limit which is determined by the size of a single calibration grid (i.e. 125 mm x 125 mm). For points B and C (points in the mid-plane and closer to the root), the load points fell within the estimated region as far as the y-direction was concerned but were measured towards the corners in the x-direction. This is attributed to the internal stresses and curvature playing a role on the measured strain, for example see the anomalous behaviour in the region around point (0.6,0.7). On average for all the cases, the test points were located within a region of  $(x,y) = (57.6 \pm 1, 67.5 \pm 1)$  mm within a (1000,1000) mm section.

With a sparse calibration grid, it usually happens that two or more points are closer to 100 on the colour bar. The test point in such cases is estimated to be between these points and typically on or within the black region. In this study, we considered a linear change between these reference points and hence the estimated regions are not curved in form. In order to achieve higher spatial resolution and accuracy, more data points need to be added to the library or alternatively through an enhanced algorithm. The calculated point is added as a new data point by the learning algorithm after each test. This helps in building a database of information pertaining to different tests and hence developing a finer grid.

### 5.2 Coarser grid

Furthermore, a second test was conducted but this time using a coarser (3x3) grid, refer to Sect. 4.2.2, to understand the effect of missing calibration points. This change sees the increase in error of position sensing. The error shoots up to 6% and 18% in the x and y-directions, respectively,

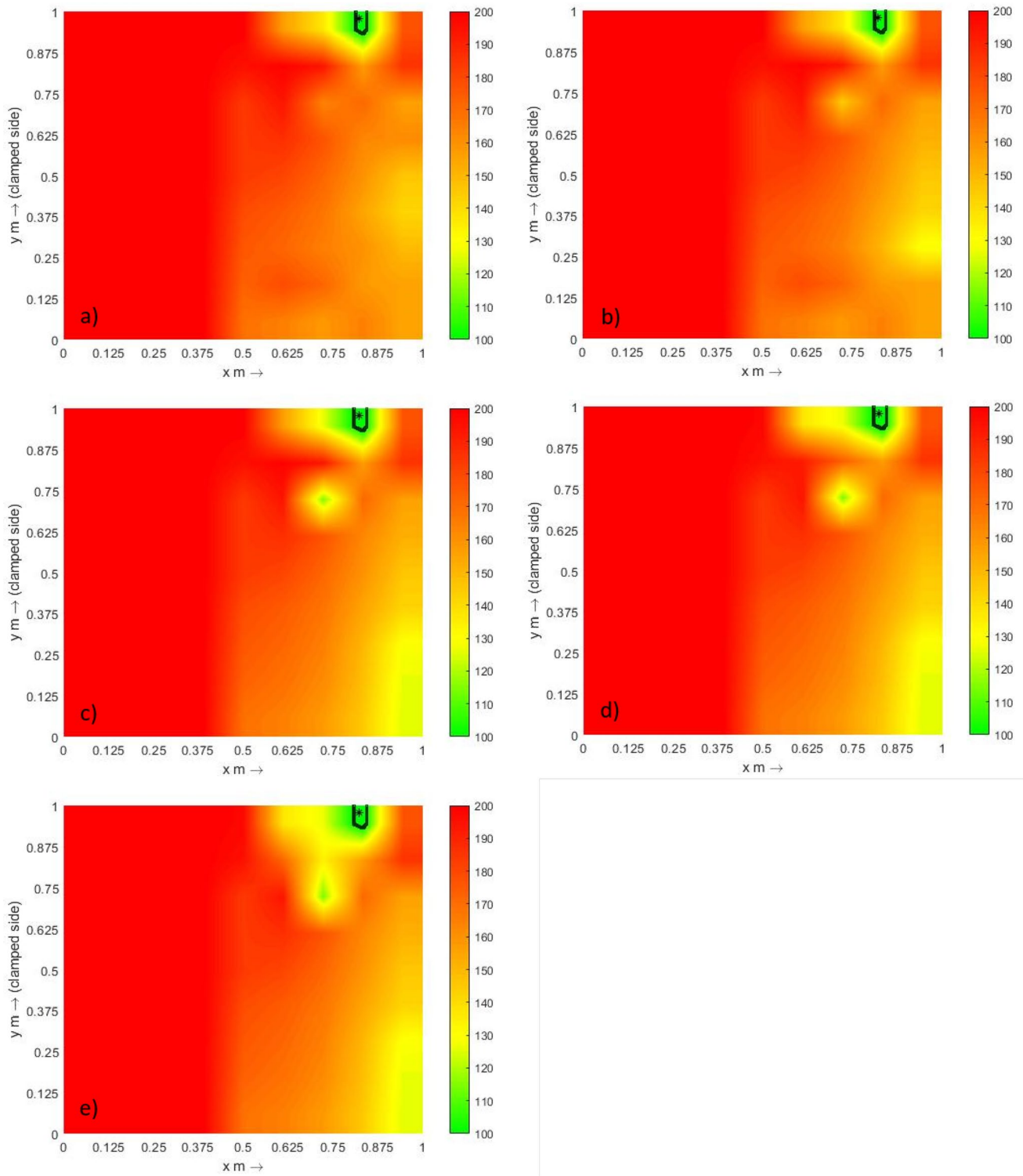


**Fig. 12** Estimated region of the position of load applied for test point A using a finer grid with a deflection of **a** 5 mm, **b** 10 mm, **c** 15 mm, **d** 20 mm and **e** 25 mm. Asterisk marks the actual position of applied load

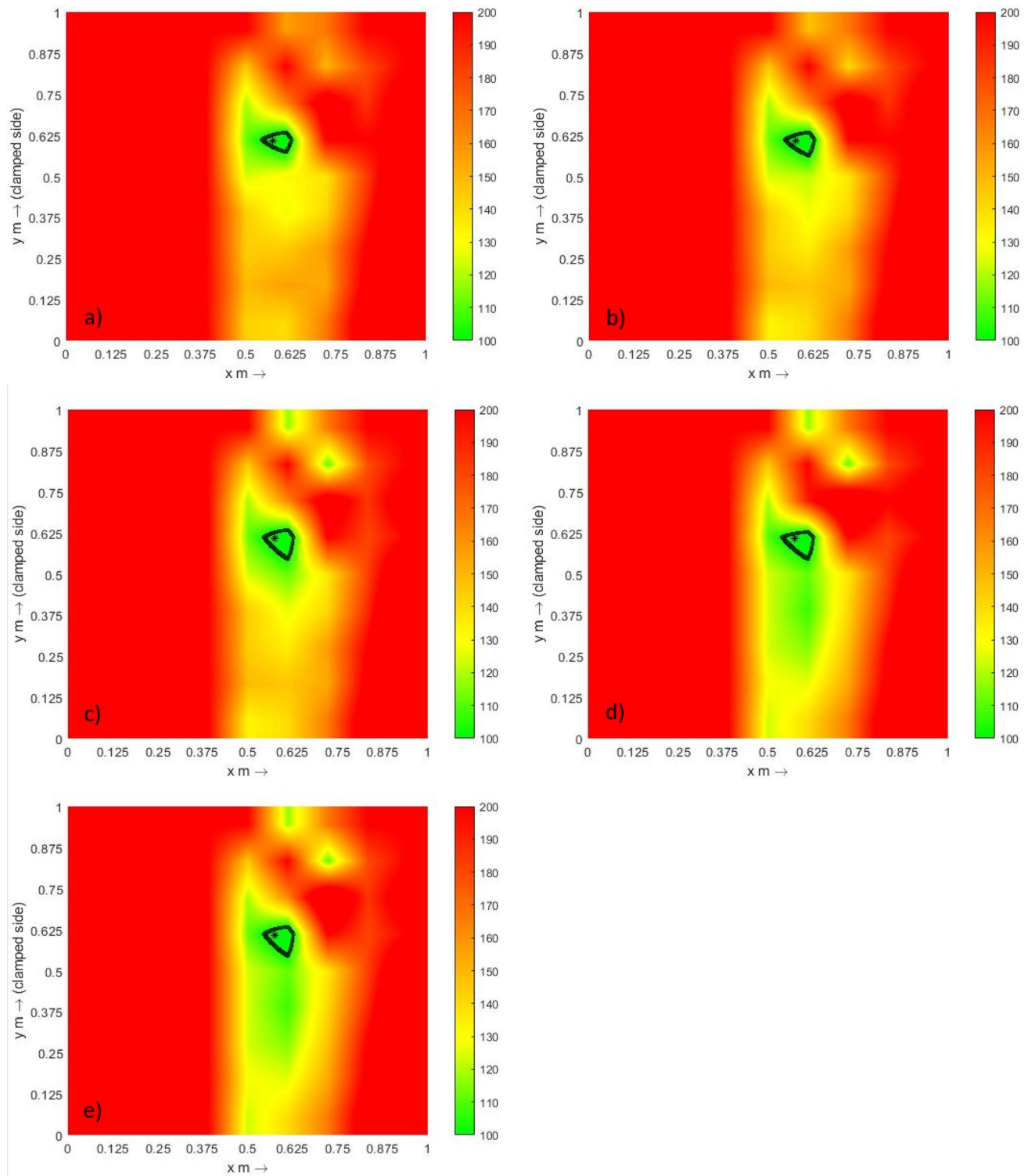


**Fig. 13** Estimated region of the position of load applied for test point B using a finer grid with a deflection of **a** 5 mm, **b** 10 mm, **c** 15 mm, **d** 20 mm and **e** 25 mm. Asterisk marks the actual position of applied load

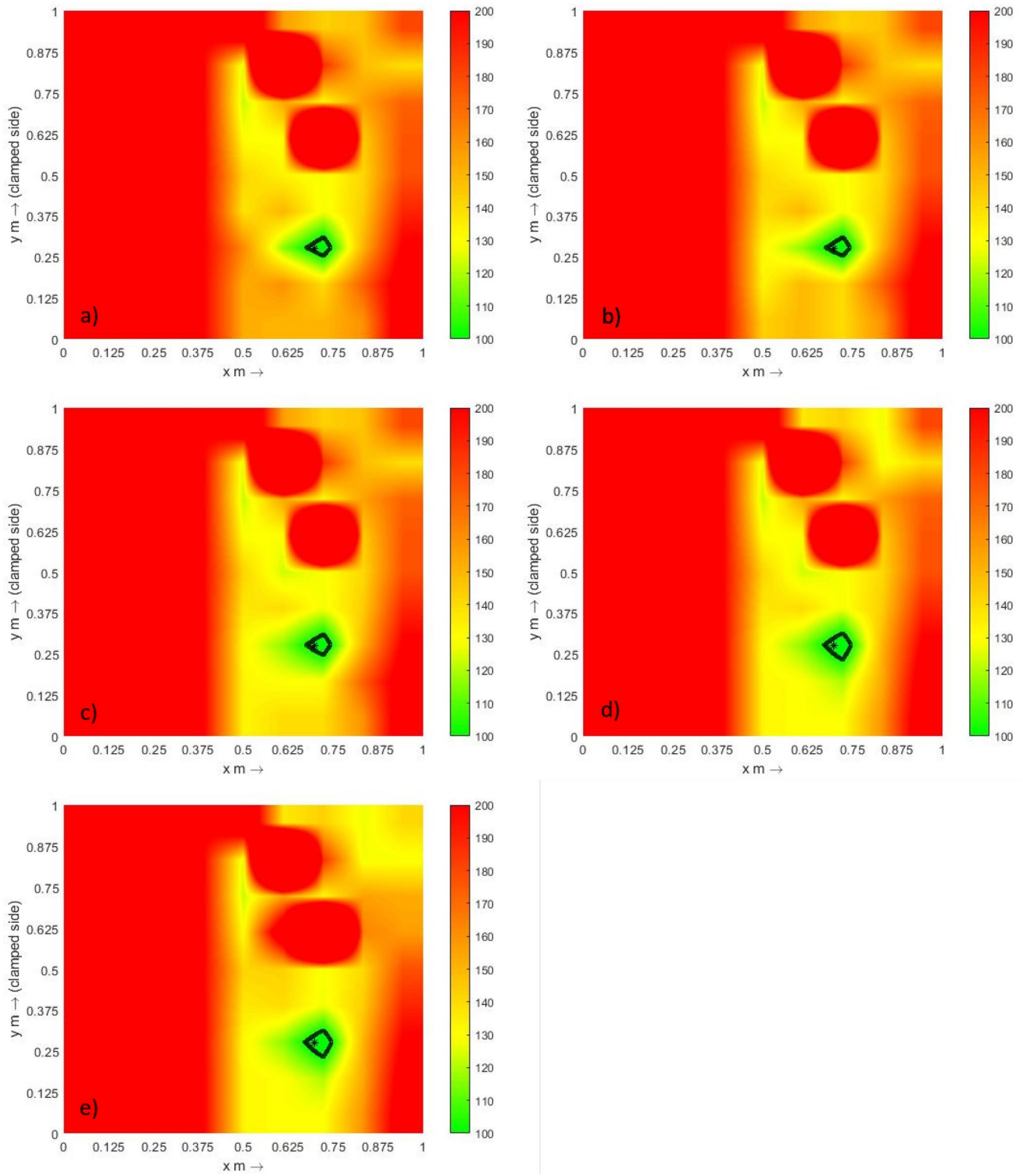


**Fig. 14** Estimated region of the position of load applied for test point C using a finer grid with a deflection of **a** 5 mm, **b** 10 mm, **c** 15 mm, **d** 20 mm and **e** 25 mm. Asterisk marks the actual position of applied load

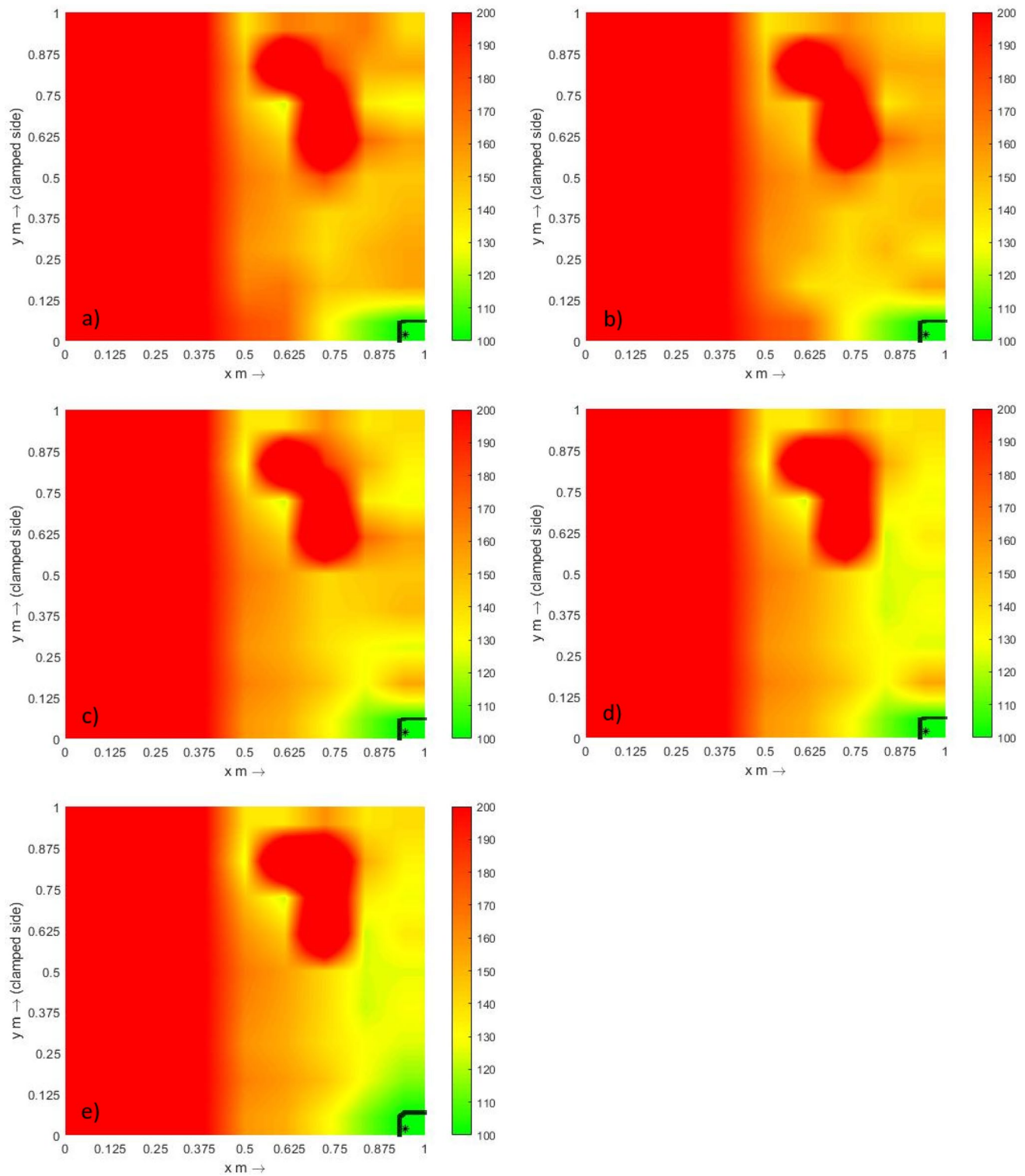


**Fig. 15** Estimated region of the position of load applied for test point D using a finer grid with a deflection of **a** 5 mm, **b** 10 mm, **c** 15 mm, **d** 20 mm and **e** 25 mm. Asterisk marks the actual position of applied load

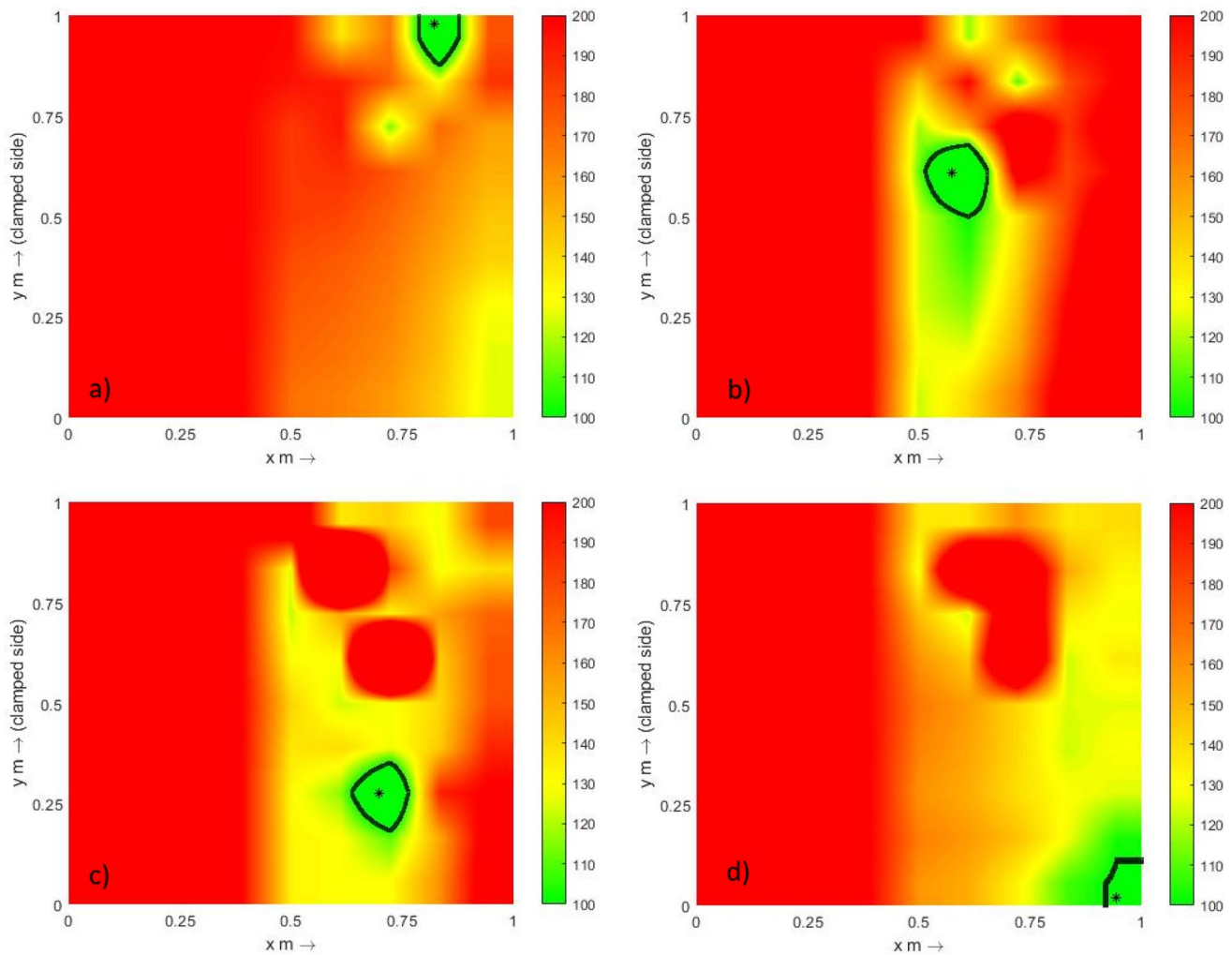


**Fig. 16** Estimated region of the position of load applied using a coarser grid with a deflection of 20 mm for test points **a** A, **b** B, **c** C and **d** D. Asterisk marks the actual position of applied load

calculated by the difference between the estimated and true position. This gives an error in the x-y plane of about 20%.

### 5.2.1 Data point number dependency

As mentioned earlier, the algorithm updates its library with every test and the results get refined each time. To depict the refinement in results when the algorithm updates the library, a third test was carried out with the new grid. The results for arbitrary locations A to D are shown in Fig. 16. For this test, only deflections of 20 mm are shown.

The results are not as accurate as the first test due to fewer calibration points. The estimated regions are larger due to the scarcity of calibration points but nevertheless fall within the estimated region. Similar to the finer grid case for A-D (see Sect. 5.1), the size of the estimated region

is in the range of a single calibration grid (in this case: 250 mm x 333 mm). In this test, there are three calibration points along a 500 mm length (x direction) and there are again three along the y-axis but across a 1000 mm section, which explains the greater error in y-axis location prediction.

## 6 Discussion

This work demonstrates the working of a novel sensing method to predict the position of load on a plate in 2 dimensions within specified boundary conditions.

The plate was firmly clamped at one end and left free at the other end to form a vertical cantilever. The plate had residual stresses and uneven curvatures that arose during the cutting and bolting process. This did not have an effect on the static tests as all sensors were reset at the

interrogator prior to every test to have a good comparison with different loading cases. As the loading point of interest was in the plate's free half region, the measurements did not include data for points from the clamp ( $x = 0$  to  $x = 0.5$  m). All calibration and test points were chosen to be within the region  $x = 500$  mm to 1000 mm. The calibration points consisted of 45 equally spaced markers that formed a 5x9 grid within this region.

The following paragraph addresses inaccuracies in the experimental setup and possible error sources that may directly or indirectly affect the measurements.

The sections from S1 to S2 and S3 to S4 of the fibre are manually bonded and are estimated to have a  $\pm 1^\circ$  variation from the line parallel to the x-axis. Furthermore, for measurements along the centreline of the plate, there is an average of 25% difference for  $\Delta L$  and  $\varepsilon$  readings between the grating pairs. Apart from irregularities in the plate forcing it to bend unevenly, this difference is also caused due to inaccuracies during fibre layup, orientation, as well as difference in lengths between the grating pairs. The position of each of the gratings specified by the manufacturer is an estimate and can be more than three times the length of the grating itself. In order to have an estimate of this location, a study on the side lobes of each grating's spectrum must be carried out [34]. Although all these difference contribute to a high error, it does not affect the final position sensing as the calibration (Sect. 4.1) is also done under the same fibre/sensor design settings. This also highlights the importance of the initial calibration procedure.

The thermal expansion of the adhesive and the plate together affects the temperature response of the gratings. These slow changes are easily filtered out at the interrogator level and are not present in the final signal. As a result, the strain response of the gratings was constant over time. Furthermore, this was verified as the experiments were conducted in a controlled environment where the temperature variation was measured to be small enough (within  $\pm 0.5^\circ$ ) that it had negligible effect on the final readings.

Improper or incomplete bonding of the fibre to the plate would influence the measurements. It is noteworthy that throughout the test campaign there was no debonding observed between the fibre and the plate.

Overall a uniform trend is noticed in cases A to D. Although the actual loading point (asterisk) is within the estimated region, lower deflection magnitudes gave more accurate predictions. The stresses in the plate are higher for higher loads, and this is seen by the gradual shift of the colours from red to (200 on the colour map) towards green (100 in the colour map). This is indicative of an increasing error map across the plate which is also

attributed to the residual stresses and uneven curvature as discussed in Sect. 3.1.

Assuming the plate has a perfect bending profile without the presence of residual stresses or uneven curvature, we would observe a single green region with a black spot marking the region of interest. This means the absence of any colour corresponding to 120 and above on the colour map. Due to the erratic stress distributions in the plate and uneven curvature that was caused due to the cutting and bolting process, we observe rather an unevenly spread-out combination of green, yellow, orange and red regions across the plate. A follow-up work could be a study to understand the emergence of these random spread out coloured regions and to study there patterns for different deflection cases. These data could provide vital information on the curvature, profile and geometry of the structure under consideration.

Although the FBG sensors are able to differentiate tension and compression, complex bending including higher order plate bending modes is not considered in this work. This complex bending was predominantly identified in the region closer to the clamp ( $x = 0$  mm to  $x = 500$  mm) and was not recorded or investigated further as it was out of the scope of this work. This can also be verified by noting that test point B has the highest error, which was expected as it is closer to the clamp than the other test points.

This method has been adopted to be able to accommodate structures whose structural response behaviour would be difficult to capture through analytical models.

## 7 Conclusion

This work presents the principles, design and application of a novel optical sensing method for point loading position estimation of a square cantilever plate.

The research successfully demonstrates the capability of a novel hybrid sensing principle involving a combination of fibre Bragg grating and fibre Bragg grating pair sensing for the deflection position measurement. This study also demonstrates that by using just four gratings, it is possible to estimate the position of the applied load in two dimensions. This is in line with the aim of using the least number of gratings possible for the estimation. On the other hand, the use of additional gratings may have an influence on the accuracy but a study on the optimum grating number is not looked into in this study.

The approach is also able to determine the deflection magnitude based on the calibration procedure. The algorithm used accurately measures the position of an applied load on a 1 m<sup>2</sup> cantilever plate with an accuracy of within



a (57,67) mm region in x and y directions, respectively. For this study, the finer grid was chosen to have 45 calibration points. To achieve an ideal grid spacing for more accurate predictions, a further grid-size convergence study would be required. The probable sources of inaccuracies are identified, and the estimated results are noted to have at most 9% error.

The demonstrated technique shows a good potential for the analysis of more complex structures. The SmartX wing from the wider project consists of independent morphing sections for which load monitoring is crucial throughout its flight regime. The complex behaviour of these sections is due to the way the morphing is achieved. This requires a simple yet robust health monitoring system to keep track of the shape while in flight. Our future work will be in the direction of load monitoring of this morphing smart wing section and demonstrator tests.

**Acknowledgements** This work is part of the strategic project SmartX in the Aerospace Structures and Materials Department, Faculty of Aerospace Engineering, Delft University of Technology. The SmartX project is focussed on the design and development of smart wing technology.

**Funding** This research was funded and supported by the Aerospace Structures and Materials (ASM) Department of the Aerospace Engineering faculty, Delft University of Technology.

#### Declarations

**Conflict of interest** On behalf of all authors, the corresponding author states that there is no conflict of interest.

**Conflicts of interest/Competing interests:** The authors declare that they have no conflict of interest.

**Availability of data and material:** The data pertaining to this work are available on request.

**Code availability:** Not applicable.

**Authors' contributions:** Both authors contributed to the study conception and design. Experimental setup, data collection and analysis were performed by Nakash Nazeer. The first draft of the manuscript was written by Nakash Nazeer. Both authors read and approved the final manuscript. Roger M. Groves supervised the whole study and approved the work for submission to Springer's SN Applied Sciences journal.

**Open Access** This article is licensed under a Creative Commons Attribution 4.0 International License, which permits use, sharing, adaptation, distribution and reproduction in any medium or format, as long as you give appropriate credit to the original author(s) and the source, provide a link to the Creative Commons licence, and indicate if changes were made. The images or other third party material in this article are included in the article's Creative Commons licence, unless indicated otherwise in a credit line to the material. If material is not included in the article's Creative Commons licence and your intended use is not permitted by statutory regulation or exceeds the permitted use, you will need to obtain permission directly from the copyright

holder. To view a copy of this licence, visit <http://creativecommons.org/licenses/by/4.0/>.

## References

1. Friebele E, Askins C, Bosse A, Kersey A, Patrick H, Pogue W, Putnam M, Simon W, Tasker F, Vincent W, Vohra S (1999) Optical fiber sensors for spacecraft applications. *Smart Mater Struct* 8:813
2. Giurgiutiu V (2015) Structural health monitoring of aerospace composites. Academic Press, Cambridge
3. Yang W, Peng Z, Wei K, Tian W (2016) Structural health monitoring of composite wind turbine blades: challenges and issues and potential solutions. *IET Renew Power Gen* 11:411–416
4. Wang P, Tian X, Peng T, Luo Y (2018) A review of the state-of-the-art developments in the field monitoring of offshore structures. *Ocean Eng* 147:148–164
5. Li HN, Ren L, Jia ZG, Yi TH, Li DS (2016) State-of-the-art in structural health monitoring of large and complex civil infrastructures. *J Civil Struct Health Monitor* 6(1):3–16
6. Forbes B, Vlachopoulos N, Hyett AJ, Diederichs MS (2017) A new optical sensing technique for monitoring shear of rock bolts. *Tunnell Undergr Space Technol* 66:34–46
7. Tennyson R, Coroy T, Duck G, Manuelpillai G, Mulvihill P, Cooper D, Smith P, Mufti A, Jalali S (2011) Fibre optic sensors in civil engineering structures. *Can J Civil Eng* 27:880–889
8. Yuan FG (ed) (2016) Structural Health Monitoring (SHM) in aerospace Structures. Woodhead Publishing, Cambridge
9. Ma Z, Chen X (2018) Fiber Bragg gratings sensors for aircraft wing shape measurement: recent applications and technical analysis. *Sensors* 19:55
10. Boller C (2013) Structural health monitoring - its association and use. Springer, New York
11. Noll TE, Brown JM, Perez-Davis ME, Ishmael SD, Tiffany GC, Gaier M (2004) Investigation of the helios prototype aircraft mishap. NASA
12. Ko W, Richards W, Fleischer V (2009) Applications of the ko displacement theory to the deformed shape predictions of the doubly-tapered ikhona wing (NASA/TP-2009-214652)
13. Jutte CV, Ko WL, Stephens CA, Bakalyar JA, Richards WL, Parker AR (2011) Deformed shape calculation of a full-scale wing using fiber optic strain data from a ground loads test (NASA/TP-2011-215975)
14. Udd E, Spillman W (2011) Fiber optic sensors: an introduction for engineers and scientists, 2nd edn. Wiley, Hoboken
15. Roesthuis R, Kemp M, Dobbelsteen J, Misra S (2014) Three-dimensional needle shape reconstruction using an array of fiber bragg grating sensors. *IEEE/ASME Transactions Mechatron* 19:1–12
16. Parent F, Loranger S, Kanti Mandal K, Lambin lezzi V, Lapointe J, Boisvert JS, Baiad MD, Kadoury S, Kashyap R (2017) Enhancement of accuracy in shape sensing of surgical needles using optical frequency domain reflectometry in optical fibers. *Biomed Opt Exp* 8:2210–2221
17. Molardi C, Issatayeva A, Beisenova A, Blanc W, Tosi D (2019) 3D shape sensing medical needle based on the multiplexing of optical backscattering reflectometry. *Proc SPIE Int Soc Opt Photon* 11191:27–32
18. Murayama H, Tachibana K, Hirano Y, Igawa H, Kageyama K, Uzawa K, Nakamura T (2012) Distributed strain and load monitoring of 6 m composite wing structure by FBG arrays and long-length FBGs. *Proc SPIE International Conference on Optical Fiber Sensors* 8421:440–443
19. De Mooij C, Martinez M, Benedictus R (2016) Sensor fusion for shape sensing: theory and numerical results. 27th International Conference on Adaptive Structures and Technologies: Lake George, USA

20. Gherlone M, Cerracchio P, Mattone M (2018) Shape sensing methods: review and experimental comparison on a wing-shaped plate. *Prog Aerosp Sci* 99:14–26
21. Mizutani Y, Groves RM (2011) Multi-functional measurement using a single FBG sensor. *Exp Mech* 51(9):1489–1498
22. Rauf A, Zhao J, Jiang B (2013) High-sensitivity bend angle measurements using optical fiber gratings. *Appl. Opt.* 52(21):5072–5078
23. Jones RT, Bellemore DG, Berkoff TA, Sirkis JS, Davis MA, Putnam MA, Friebele EJ, Kersey AD (1998) Determination of cantilever plate shapes using wavelength division multiplexed fiber Bragg grating sensors and a least-squares strain-fitting algorithm. *Smart Mater Struct* 7(2):178–188
24. Flockhart GMH, MacPherson WN, Barton JS, Jones JDC, Zhang L, Bennion I (2003) Two-axis bend measurement with Bragg gratings in multicore optical fiber. *Opt. Lett.* 28(6):387–389
25. Gander M, Macpherson W, Mcbride R, Jones J, Zhang L, Bennion I, Blanchard P, Burnett J, Greenaway A (2000) Bend measurement using Bragg gratings in multicore fibre. *Electron Lett* 36:120–121
26. Westbrook PS, Kremp T, Feder KS, Ko W, Monberg EM, Wu H, Simoff DA, Taunay TF, Ortiz RM (2017) Continuous multicore optical fiber grating arrays for distributed sensing applications. *J Lightwave Technol* 35(6):1248–1252
27. Nicolas MJ, Sullivan RW, Richards WL (2016) Large scale applications using FBG sensors: determination of in-flight loads and shape of a composite aircraft wing. *Aerospace* 3(3):18
28. Nazeer N, Groves RM, Benedictus R (2019) Simultaneous position and displacement sensing using two fibre Bragg grating sensors. *Proc SPIE Smart Structures + Nondestructive Evaluation* 10970:109701Z–1-109701Z–8
29. Hill KO, Meltz G (1997) Fiber bragg grating technology fundamentals and overview. *J Lightwave Technol* 15(8):1263–1276
30. Kashyap R (2010) Chapter 3 Fabrication of Bragg Gratings, chap Innovation and Intellectual Property Rights. Academic Press, Boston pp 53–118
31. Kersey AD, Davis MA, Patrick HJ, LeBlanc M, Koo KP, Askins CG, Putnam MA, Friebele EJ (1997) Fiber grating sensors. *J Lightwave Technol* 15(8):1442–1463
32. Kersey AD (1996) A review of recent developments in fiber optic sensor technology. *Opt Fiber Technol* 2(3):291–317
33. Gruca G, Rijnveld N (2018) Ep3335014 - optical fiber-based sensor system. Publication number 3335014
34. Rajabzadeh A, Heusdens R, Hendriks RC, Groves RM (2019) A method for determining the length of FBG sensors accurately. *IEEE Photon Technol Lett* 31(2):197–200

**Publisher's Note** Springer Nature remains neutral with regard to jurisdictional claims in published maps and institutional affiliations.